Additive Manufacturing 24 (2018) 639–646

Contents lists available at ScienceDirect

Additive Manufacturing

journal homepage: www.elsevier.com/locate/addma

Full Length Article

Continuous wave vs pulsed wave laser emission in selective laser melting of AlSi10Mg parts with industrial optimized process parameters: Microstructure and mechanical behaviour

C.A. Biffi*, J. Fiocchi, P. Bassani, A. Tuissi

National Research Council, Institute of Condensed Matter Chemistry and Technologies for Energy, Unit of Lecco, CNR ICMATE, Via Previati 1/E, 23900 Lecco, Italy

ARTICLE INFO

Keywords:
Selective laser melting
Additive manufacturing
Al alloy
Microstructure
Mechanical properties

ABSTRACT

Currently, selective laser melting (SLM) is among the most widespread of the additive manufacturing (AM) technologies. Commercially available SLM systems can offer both continuous wave (CW) and pulsed wave (PW) emissions of the laser power. It has been demonstrated that relative density and geometric features can be affected by the laser emission parameters, but their effects on the material properties have not yet been investigated. In this study, specimens were produced from the same AlSi10Mg powder using two commercially available SLM machines operating with CW and PW emissions. Optimal process conditions were used, as indicated by the SLM suppliers. This choice was made to provide the most effective comparison between the material performances obtained using different industrial SLM systems. The specimen microstructures were investigated using scanning electron microscopy coupled with electron backscatter diffraction analysis. Moreover, thermal analysis, microhardness measurements, and compression tests were performed to investigate the thermal and mechanical properties. It was revealed that a slightly finer microstructure was obtained using the PW laser, while the increased thermal load during CW laser melting resulted in larger liquid pools, enhanced phase modifications, and better mechanical properties.

1. Introduction

Currently, selective laser melting (SLM) processes have reached a promising industrial diffusion. The producers of SLM machines offer industrial systems, which differ from each other in their powder deposition methods, laser scanning strategies, laser power, number of laser sources, building chamber size, atmosphere composition, and preheating temperature. Moreover, every producer offers a different consolidated set of process parameters for each powder type.

However, one of the most important characteristics for laser material processing is the laser beam emission type, i.e. continuous wave (CW) or pulsed wave (PW). As the laser beam is the heat source used to locally melt the single powder layer in SLM processes, the temporal distribution of available power must be considered a key parameter. In fact, heating and cooling rates are notably linked to the thermal history of the laser emission. Similar effects were observed in laser welding processes of different alloys such as steels and aluminium alloys [1–3]. Demir et al. investigated the effect of the exposure time and pulse overlapping on a maraging steel [4], and they found that a CW laser is preferable for producing fully dense large parts, while PW is more suitable for thin and precise structures. Most of the commercially available SLM systems, like EOS, Concept Laser, SLM Solutions, Trumpf and Sisma adopt CW lasers while just Renishaw offer the PW laser mode in the SLM equipment.

The production of aluminium alloy parts through additive manufacturing (AM), once considered a challenge owing to the surface oxide layer, high reflectivity, and high thermal conductivity of the material, has now reached a certain industrial maturity, and has proven particularly attractive in the automotive and aerospace fields. To date, most of the scientific investigations of AM with aluminium powders have used SLM machines based on CW lasers [5–9]. In this respect, significant effort has been expended to optimise the process parameters for producing fully dense aluminium parts with CW lasers [5–7,10–12]. However, it has been reported that pulsed lasers may be more suitable for SLM, as they are able to induce good metallurgical bonding between layers with a smaller heat-affected zone [13–15]. Some attempts at using pulsed lasers for producing steel, titanium, and tungsten parts have been reported [16–20]; the pulsed lasers generated high power densities, giving rise to vaporisation and a recoil effect, and resulting in lower average power usage. A limited number of studies have explored

* Corresponding author.
E-mail address: carloalberto.biffi@cnr.it (C.A. Biffi).

https://doi.org/10.1016/j.addma.2018.10.021
Received 8 August 2018; Received in revised form 18 September 2018; Accepted 12 October 2018
Available online 28 October 2018

Table 1
Chemical composition of the AlSi10Mg powder (wt. %) according to specifications (1st row) and as measured by EDS (2nd row).

Si	Mg	Cu	Ni	Fe	Mn	Ti	Al
10	0.4	< 0.25	< 0.05	< 0.25	< 0.1	< 0.15	bal.
9.22	0.41	–	–	0.16	–	–	bal.

the effects of using pulsed lasers for SLM of aluminium components [21,22]. To the best of the authors' knowledge, only one study [23] has performed a numerical comparison of CW and PW lasers for producing aluminium parts. Another study focused on comparing the effect of CW and PW laser power emissions on the aspect ratio of the liquid pool and the material deposition rate using homemade SLM equipment with AISI 316 L powder [24]. However, no systematic experimental comparison between the effects of CW and PW lasers on the microstructure and mechanical properties of materials has been conducted using optimised process conditions and commercially available systems in the available literature.

The present study aims to investigate the effect of using continuous or pulsed lasers on the microstructure and mechanical properties of AlSi10Mg specimens produced with SLM. The feasibility ranges for many parameters or even their definitions (i.e. powder layer thickness, exposure time, and laser travel speed) are quite different for the two systems, which significantly limits the usefulness of comparisons made by varying single/multiple parameters. Hence, to perform an industrial and reliable comparison between the two emission modes, samples were built with two commercial machines using optimal process parameters, as suggested by the supplier of each SLM system. The mechanical, microstructural, and thermal properties of the fabricated parts were then investigated.

2. Materials and methods

Commercially available gas atomised AlSi10Mg powder was used, and its composition is reported in Table 1. The composition was confirmed using electron dispersive spectroscopy, and was found to be consistent with the supplier's specification, as presented in Table 1. The powder morphology was observed using optical and scanning electron microscopy (Fig. 1), and was found to be mainly spherical with a few satellites. The internal microstructure was characterised by silicon segregation, and exhibited a typical fine dendritic structure. Powder diameters ranged from 20 to 63 µm, with an average size of approximately 45 µm.

The powder was processed using two SLM machines: (i) Renishaw AM 250 system, equipped with a PW ytterbium fibre laser; and (ii) SLM Solutions SLM 500 system, equipped with a 400 W CW fibre laser. Samples were fabricated in the form of small parallelepipeds lying on the building plate. The process parameters were suggested by the equipment suppliers, and are reported in Table 2.

Table 2
Process parameters used for the SLM building of the AlSi10Mg samples.

Laser emission Parameter	PW laser Value	CW laser Value
Laser power (W)	300	350
Build plate temperature (°C)	170	150
Exposure time (µs)	120	–
Laser travel speed (mm/s)	–	1150
Point distance (µm)	130	–
Spot size (µm)	130	80
Hatch distance (µm)	140	170
Layer thickness (µm)	25	50
Atmosphere	Argon	Argon

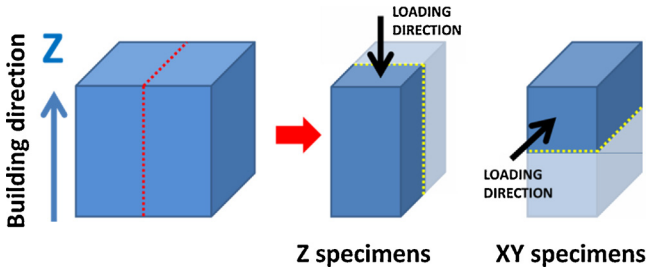

Fig. 2. Schematics depicting specimen geometry for compression testing with indication of the building direction and loading direction during compression tests.

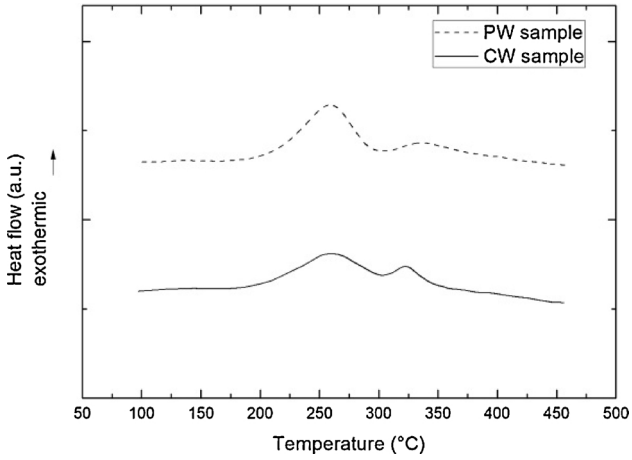

Fig. 3. DSC analyses of as built samples, produced using PW and CW laser emission.

Prior to any further analysis the density of the produced samples was measured by means of Archimede's principle and was found to be fully satisfactory. Both production systems allowed to obtain densities

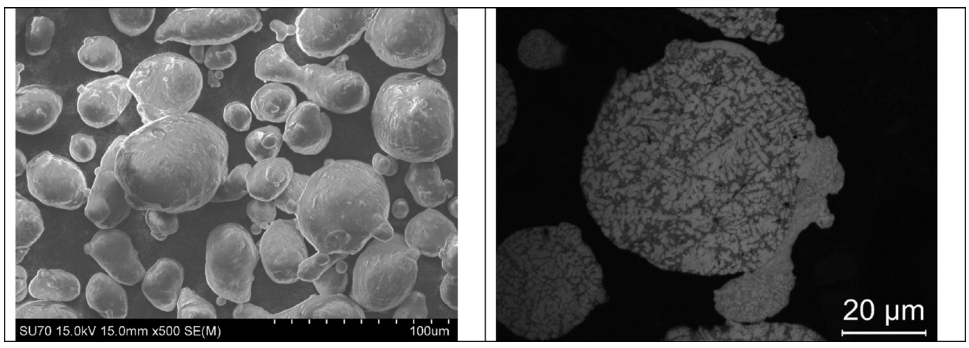

Fig. 1. SEM and OM micrographs of the used AlSi10Mg powder.

Table 3
Characteristic temperatures, transformation enthalpies and activation energies obtained from DSC analyses.

	PW laser			CW laser		
	Peak temperature (°C)	Transformation enthalpy (mJ/mg)	Activation energy (KJ/mol)	Peak temperature (°C)	Transformation enthalpy (mJ/mg)	Activation energy (KJ/mol)
Peak 1	262,3	25,2	110	263,3	22,6	101
Peak 2	324,0	10,1	165	322,3	5,5	181

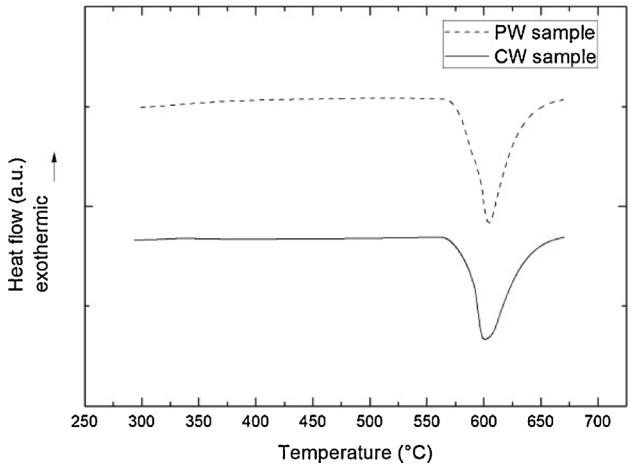

Fig. 4. DTA analyses of as built samples, produced using PW and CW laser emission.

Table 4
Characteristic temperatures revealed by DTA analyses.

PW laser built sample		CW laser built sample	
Onset temperature (°C)	Peak temperature (°C)	Onset temperature (°C)	Peak temperature (°C)
570,4	604,7	568,6	601,1

higher than 99.5%. A thermal analysis was conducted to evaluate the critical points of the built samples. For this purpose, two systems were used: (i) differential thermal analysis (DTA, model Q600, TA Instruments) in the temperature range of 200–700 °C, with a heating rate of 20 °C/min for measurement of the melting point; and (ii) differential scanning calorimetry (DSC, model Seiko DSC220C) to detect thermal signals related to phase transformations and precipitation phenomena, performed in a temperature range of 0–500 °C with a heating rate of 10 °C/min. DSC results were also used to compute the activation energies of the precipitation phenomena using Kissinger's method [25]. Kissinger's method is based on a number of assumptions, including that the equilibrium states resulting from transformations are independent of the temperature, and that only transformations involving a single thermally activated process are considered. Nevertheless, widespread consensus about the applicability of Kissinger's method for solid-state precipitation phenomena in metallic alloys was found in the literature [26–29].

The microstructure of the built specimens was evaluated with optical microscopy (OM, model Leitz Aristomet) and scanning electron microscopy (SEM, Leo1430 Zeiss; FEG SEM, SU70 Hitachi). The crystalline texture of the specimens was investigated using electron backscatter diffraction (EBSD) performed on XZ sections (Oxford INCA Crystal, with SEM operating at 20 kV, step sizes of 0.5–2 μm depending on the magnification). Mechanical properties were evaluated using microhardness measurements (Future Tech Corporation FM-700, 200 g load applied for 15 s) and compression tests (MTS 2/M universal testing machine, equipped with a 10 kN load cell). Prismatic specimens with an almost square base of approximately 3 x 3 mm were machined from the built samples, with the main axis parallel to the building direction (Z-type specimens) or lying in the XY plane (XY specimens), as shown in Fig. 2. The height to equivalent diameter ratio of the specimens was between 1.85 and 1.95. Three specimens of each type were compressed with a cross-head speed of 0.05 mm/min, corresponding to a strain rate of about 0.65%/min. Tests along the Z-direction were stopped at 20% deformation, whilst those along the XY-direction were stopped at 15% deformation.

3. Results

3.1. Thermal analysis measurements

The low temperature thermal analysis indicates the presence of two exothermic peaks at approximately 260 °C and 320 °C, as shown in Fig. 3. These phenomena were recognised from DSC scans in a previous work [30], and are related to the precipitation of Mg_2Si particles and to the rupture and spheroidisation of the Si network, respectively. Peak temperatures, transformation enthalpies, and activation energies are listed in Table 3. It can be observed that no remarkable variation in peak temperatures was induced by the use of different laser emission modes. On the other hand, the shape of the peaks varied slightly between the samples; the peaks overlapped more in the CW sample. A clear trend in the transformation enthalpies for both process types was also noted. In samples built using the CW laser, a slightly smaller amount of Mg_2Si precipitate was formed upon heating, and less silicon underwent transformation. As far as the activation energies are concerned, the difference between the computed values for Mg_2Si precipitation is negligible. On the other hand, Si spheroidisation and precipitation is shown to have a higher activation energy in the CW sample, and this variation, while small, is considered meaningful.

Results of the high temperature thermal analysis of samples produced using PW and CW laser emissions indicate that the alloy is characterised by a solidus temperature of about 570 °C, as shown in Fig. 4; this result is in good agreement with the relevant phase diagrams [31]. The thermograms of the built samples displayed a shallow hump, which is related to the melting of the eutectic Al–Si phase. No marked modification in characteristic temperatures (see Table 4) or peak shape was noted between samples built with different lasers.

3.2. Microstructural characterisation

Fig. 5a–c shows optical micrographs of the XZ section, i.e. parallel to the building direction, of the SLM-built samples. A limited amount of spherical porosities, which are due to gas entrapment, may be seen in both samples. No cracks were noted across the samples. The images clearly show a superposition of laser tracks caused by the layer-by-layer building strategy. As expected, melt pools were half-cylindrical in shape; however, marked differences can be noted between samples built using different laser emission types. The laser tracks were thinner in the sample built with the PW laser, probably due to the lower input energy and thinner layer thickness used by that machine (see Table 5). The most marked difference was in the curvature radius measured at the tip of each melt track: samples built using the PW laser showed

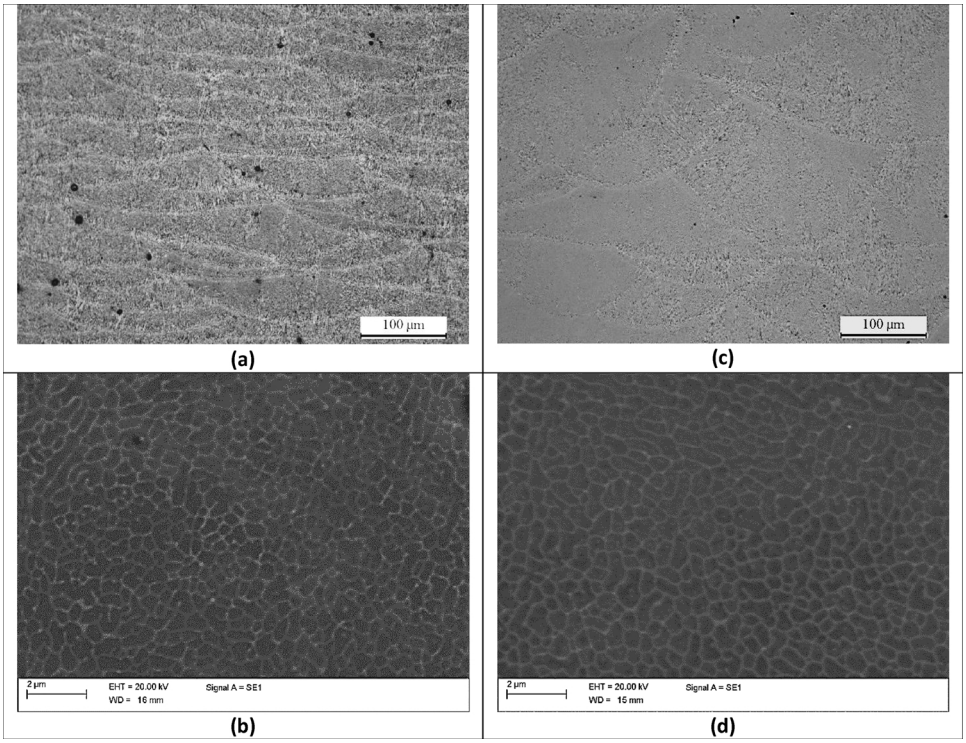

Fig. 5. OM and SEM micrographs of samples produced using PW (a, b) and CW (c, d) emission, showing XZ (a, c) and XY (b,d) views.

Table 5
Dimensions of the melt pool and extent of the HAZ in as built samples.

Geometrical features of the single melt pool	PW laser emission	CW laser emission
Melt pool height (µm)	350 (± 1,9)	630 (± 2,6)
Melt pool width (µm)	1754 (± 2,3)	1746 (± 1,8)
HAZ thickness (µm)	100 (± 0,8)	116 (± 1,7)
Curvature radius (µm)	224 (± 33)	100 (± 21)

much larger curvatures. This also caused the track widths to be similar in the two samples, even though in the CW sample they were measured at a height double that in the PW sample. This may be a result of the larger spot size used by the Renishaw machine. High magnification micrographs were obtained using SEM on the XY plane; the images in Fig. 5b–d show the fine fusion zone in the middle of the laser track. A typical eutectic cellular microstructure, induced by rapid cooling and typical of SLM processes, can be observed. Silicon formed an interconnected fine network surrounding the Si-rich aluminium matrix; this microstructure is known to positively affect the mechanical properties of the built parts. It is notable that no significant difference in microstructure type results from the use of different building strategies. The average dimensions of the Si cells in the XY plane, evaluated by the Heyn lineal intercept method according to standard ASTM E112-96 [32], were 0.52 µm (± 0.05 µm) and 0.55 µm (± 0.05 µm) in the PW and CW samples, respectively.

EBSD analyses provided additional information on the orientation of the columnar α_{Al} matrix with reference to sample direction (see Fig. 6; regions with low pattern quality or bad indexing were not considered (black pixels in images c and d)). In the vicinity of the boundaries between the melt pools, small equiaxed grains appeared, particularly in the samples built with CW emission. Large columnar grains are present in the central regions of the pools, and many of these present a < 100 > orientation along the Z-direction, i.e. the building direction.

The relative strength of this texture is different for the two types of laser emission, and it appears to be stronger in the PW sample. The ratio between the maximum and a random intensity of the peak in the (100) pole figure is 32 for the PW emission, whilst it is only 8 for the CW emission (see Fig. 6). Moreover, the PW emission is associated with a strong tendency for epitaxial growth: columnar features appear to nucleate inside one pool and then extend over the following pool. In contrast, these features are nearly absent in the sample produced using CW emission. Orientation imaging maps (OIMs) clearly show this aspect: in the PW sample, elongated grains that spread across more than one melting pool are visible, whilst in the CW sample, melting pool boundaries are easily observed.

3.3. Mechanical characterisation

The results of the compressive tests are shown in Fig. 7, and the corresponding principal features are listed in Table 6. A clear difference in the compressive behaviour of the specimens is observed. A stronger difference between the Z and XY-directions is observed in the samples produced using the PW laser emission, while the CW samples exhibit mechanical behaviour that is more similar in the two directions. The compressive strength was lower for PW-built specimens than CW-built specimens, in accordance with the hardness measurement results shown in Fig. 8. Microhardness values are higher for the CW emission than the PW emission due to the lower cooling rate experienced by CW samples. This is in good agreement with the melt pool sizes presented in Table 5. In contrast, no large difference between the XY and Z directions, particularly for samples produced using the CW emission, can be detected. All specimens showed ductile behaviour, and failure occurred by buckling, which is clearly observable after about 5% deformation. Deformation was allowed to continue until reaching 20% engineering strain for the Z samples and 15% engineering strain for the XY samples in order to observe deformation behaviour at large strains; no visible cracks appeared in any of the samples. The stress values evaluated at different strains for both directions are reported in Table 6 along with the corresponding calculated percentage differences. It should be noted that even at higher deformation levels, a greater difference between the

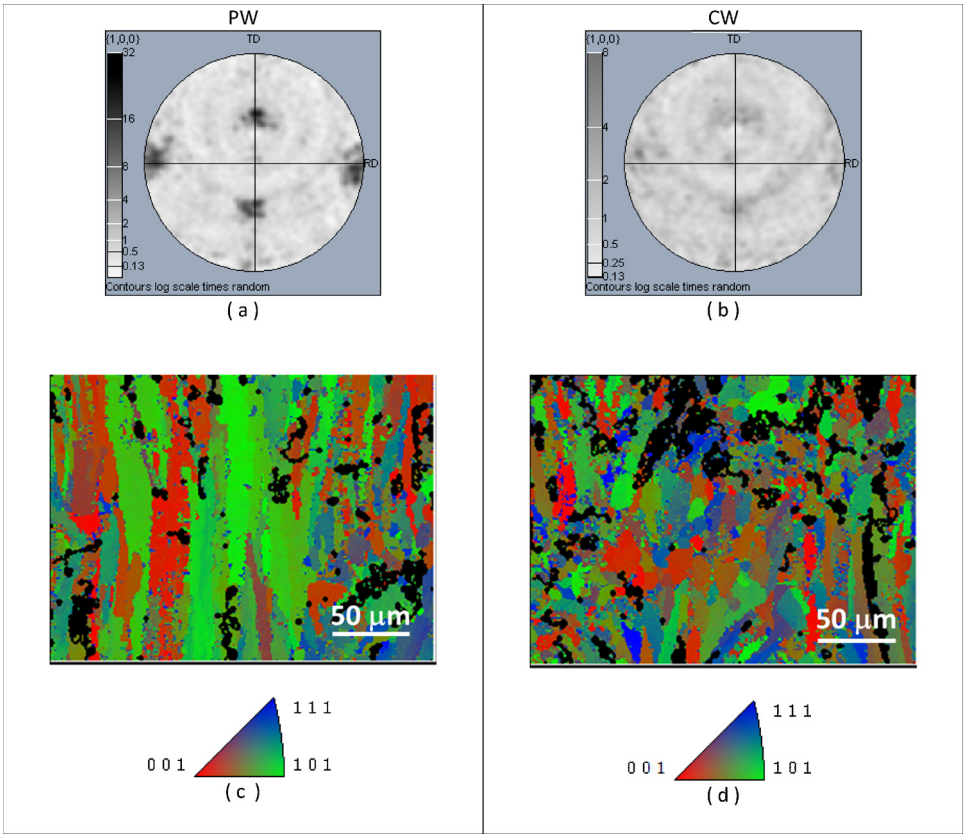

Fig. 6. (100) pole figures and OIM (referred to building direction) of samples produced using a PW (a, c) and CW (b, d) emission. Regions with low pattern quality or bad indexing were not considered (black pixels in images c and d).

XY and Z compression directions for the PW-built sample can be observed when shear deformation is relevant.

4. Discussion

The observed differences in the microstructure and mechanical properties between the investigated samples can be linked to the building strategy and process parameters, including the use of either PW or CW laser emissions (see the schematics in Fig. 9a,b). In these emission modes, the input energy is applied with very different temporal profiles, which affect the melting and subsequent cooling of the melt pool. Technological and microstructural differences resulting from laser welding have been investigated in only a few studies in the literature [1,3]. It has been reported that the width and penetration of the melt pool can vary as function of the laser emission. In details, the penetration depth can be varied with both the power density and laser mode emission (CW and PW), so the solidification and liquation mechanisms are slightly different, inducing different final properties in the joint. Schematics of the melt pool volumes occurring in CW and PW laser welding are shown in Fig. 9c and d, respectively.

The differences between the two laser emissions can be related to the energy and thermal histories induced in the material. In PW laser emission mode the liquid pool freezes between pulses, so the surface tension gradient is the one force in opposition to the keyhole formation. In addition to this, in CW mode the effect of the laser motion need to be taken into account, too. Consequently, the CW laser mode emission can provoke a large liquid pool, due to the delay of the keyhole onset [1].

The energy densities (E) of samples produced with CW and PW emissions can be calculated according to Eqs. (1) and (2) [33], respectively:

$$E = \frac{P}{v\,s\,h} + \frac{\rho}{MM}\left[a\,(T_p - T_{amb}) + b\frac{{T_p}^2 - {T_{amb}}^2}{2}\right] \quad (1)$$

$$E = \frac{P\,t_{exp}}{d\,s\,h} + \frac{\rho}{MM}\left[a\,(T_p - T_{amb}) + b\frac{{T_p}^2 - {T_{amb}}^2}{2}\right] \quad (2)$$

where P is the laser power; t_{exp} is the exposure time (i.e. t_{on} for PW or t for CW emissions); v is the scanning speed; d is the point distance; s is the hatch spacing; h is the layer thickness; ρ and MM are the theoretical mass density and the molecular mass of the material, respectively; T_{amb} and T_p are the starting ambient temperature and the build plate temperature, respectively; and a and b are thermodynamic constants of solid aluminium.

The above expressions take into account both the laser and build plate heating as energy sources. The obtained energy densities were 50.79 J/mm^3 for the CW sample and 79.12 J/mm^3 for the PW sample. In both cases, the energy input coming from the build plate temperature played a very small role compared to the laser.

Even though the energy input in the PW process is higher that applied by the CW laser, it is believed that most of the differences between the two batches resulted from the different cooling rates induced by the processing strategies. Numerical simulations performed by Ding et al. [23] showed that using a PW laser induces cooling rates which are much larger than those obtained with continuous exposure. The DSC experiments revealed that the transformation enthalpies for Mg_2Si precipitation and Si spheroidisation are higher in the PW sample. Presumably, the faster cooling in the PW sample induced a greater supersaturation of the solid solution and did not allow solute atoms to diffuse to form precipitates. This phenomenon is particularly evident for the second DSC peak. However, it may be expected that lower transformation enthalpies might also be caused by a partial loss of alloying elements due to vaporisation during processing. This hypothesis

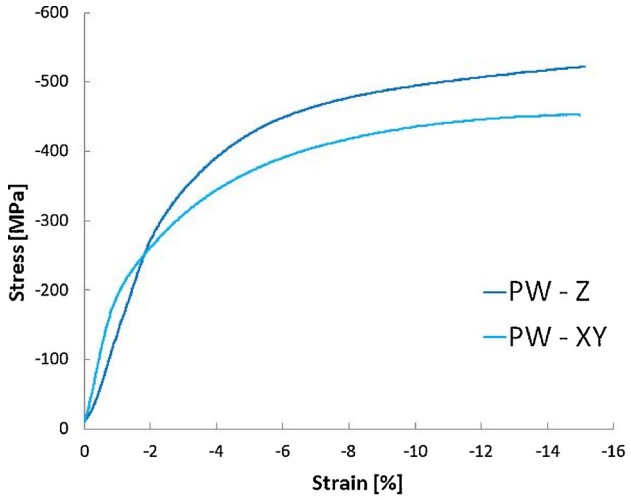

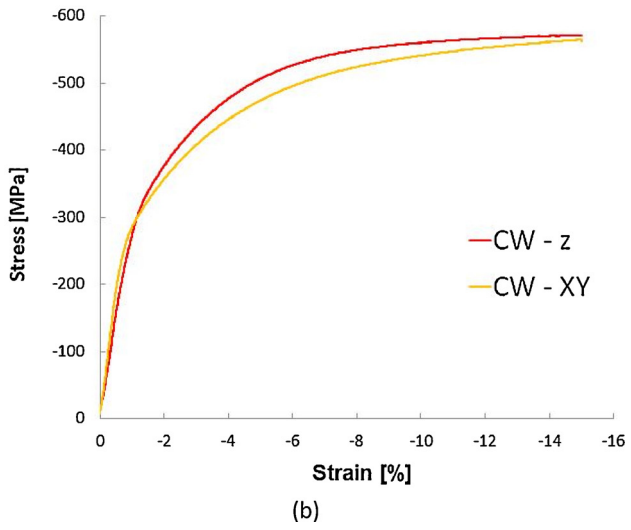

Fig. 7. Compression tests results on samples, produced using PW (a) and CW (b) laser emission, along the two principal directions.

Table 6
Main mechanical properties calculated from the compression tests.

Specimens	Yield stress (0.2% pl.def.)	Stress evaluated at the specified strain [MPa]		Stress percentage difference in different planes: XY vs. Z direction	
	[MPa]	at $\varepsilon = 5\%$	at $\varepsilon = 10\%$	at $\varepsilon = 5\%$	at $\varepsilon = 10\%$
PW-z	296 ± 20	−425.8	−494.6	14.7 %	13.6 %
PW-xy	203 ± 24	−371.2	−435.4		
CW-z	350 ± 25	−506.7	−560.0	6.7 %	3.5%
CW-xy	274 ± 20	−474.7	−541.1		

can be excluded by considering that the EDS analyses showed no variation in composition. The data also confirm that the difference between the applied energy densities is not sufficient to differentially vaporise alloying elements. Moreover, a difference in the activation energies, which are related to precipitation phenomena in the two sample batches, may be observed. Whereas no appreciable difference is apparent for Mg_2Si precipitation, Si precipitation is characterised by a lower activation energy in the PW samples. This may be explained by considering that the higher cooling rates associated with PW emission induce a larger amount of retained vacancies, which are known to play a fundamental role in enabling the diffusion of silicon atoms through

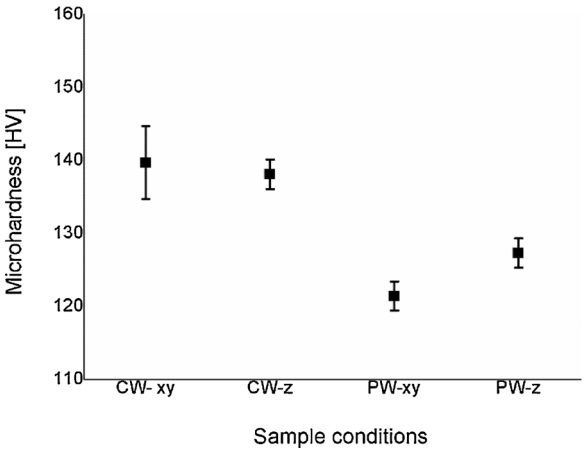

Fig. 8. Microhardness values representative of the two laser emissions in the two principal directions.

the aluminium matrix [34–36]. Hence, a smaller activation energy characterises Si precipitation and spheroidisation in the PW samples.

The microstructure of the AM AlSi10Mg indicates the presence of an interpenetrated Al matrix and Si network, which impacts the properties of the material. Unlike conventionally cast alloys, no dendritic structure is formed as a result of the high cooling rates. Silicon appears as a continuous network inside columnar grains, instead of growing as a eutectic constituent between the arm spacing. As in other fast-cooling systems, the elongated columnar grains tend to grow in the direction of the thermal gradient, i.e. the radial direction inside the melt pools, with crystals exhibiting [100] growth aligned along the direction of the maximum thermal gradient. The different thermal load and distribution results in two different shapes of the thermal gradient in CW and PW samples: the latter has higher melt pool curvature, and hence the radial directions are mostly parallel to the building direction. Consequently, the resulting microstructure is more textured. Macroscopically, this causes a more pronounced difference in the compression behaviour between the XY and Z directions for PW samples. The difference in the mean yield stress can be attributed to the different matrix microstructures resulting from the two processes. The slower cooling rate and higher extent of re-warming after primary solidification in the CW samples can explain the higher strength due to precipitation phenomena (Si particles as well as Mg_2Si precipitates). Supporting this hypothesis, the DSC analyses show a slightly lower enthalpy for such phenomena in the CW samples.

5. Conclusions

The present study investigated the effect of different laser power emission strategies, i.e. PW and CW, on the microstructure and mechanical properties of AlSi10Mg parts built with commercially available SLM systems.

The solid state transformations, which characterize the present aluminum alloy, were heavily influenced by the different thermal histories, which PW and CW samples experienced. On one hand, Mg_2Si precipitation was triggered in CW samples inducing an higher hardening, as indicated by hardness measurements. On the other hand, PW samples are characterized by lower activation energy related to Si precipitation, because of the higher cooling rate inducing larger amount of lattice defects.

As revealed by EBSD, AlSi10Mg solidifies with a columnar structure with a strong tendency for epitaxial growth. The texture intensity on a macroscopic scale is however reduced in CW samples because of the more rounded and isotropic melting pool shape. This results in a reduced influence of the building direction of samples on compression behaviour.

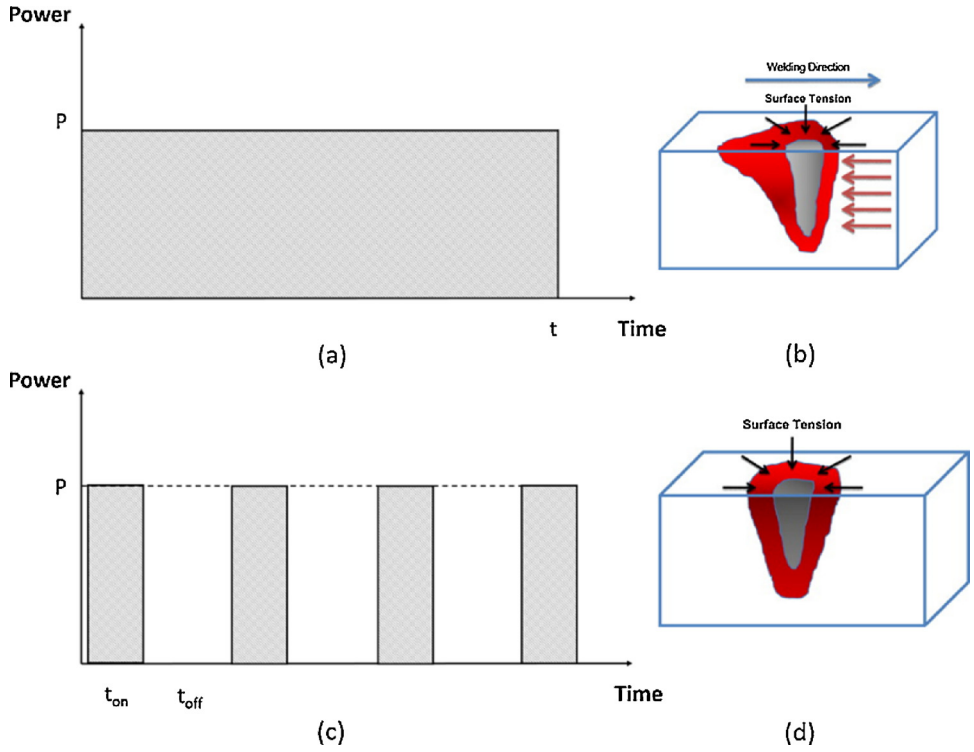

Fig. 9. Schematics of the laser emission mode and its effect in welding [1]: CW (a–b) and PW (c–d) laser emission.

Acknowledgements

The authors would like to acknowledge G. Carcano and E. Bassani from CNR ICMATE, E. Orsi, A. Consalvo and A. Penna from Renishaw Italy, E. Fella and S. Galli from Politecnico di Milano for their assistance and support in the experiments. This work was developed within the framework of 3°Accordo Quadro CNR / Regione Lombardia (FHfFC, RL N°3623 27/04/16).

References

[1] E. Assuncao, V. Williams, Comparison of continuos wave and pulsed wave laser welding effects, Opt. Lasers Eng. 51 (2013) 674–680.
[2] J. Coroado, S. Meco, S. Williams, S. Ganguly, W. Suder, L. Quintino, E. Assuncao, Fundamental understanding of the interaction of continuous wave laser with aluminum, Int. J. Adv. Manuf. Technol. 93 (2017) 3165–3174.
[3] M. Pakniat, F.M. Ghaini, M.J. Torkamany, Hot cracking in laser welding of Hastelloy X with pulsed Nd:YAG and continuous fiber lasers, Mater. Des. 106 (2016) 177–183.
[4] A.G. Demir, P. Colombo, B. Previtali, From pulsed to continuous wave emission in SLM with contemporary fiber laser sources: effect of temporal and spatial pulse overlap in part quality, Int. J. Adv. Manuf. Technol. (2017) 1–14, https://doi.org/10.1007/s00170-016-9948-7.
[5] N.T. Aboulkhair, N.M. Everitt, I. Ashcroft, C. Tuck, Reducing porosity in AlSi10Mg parts processed by selective laser melting, Addit. Manuf. 1 (2014) 77–86, https://doi.org/10.1016/j.addma.2014.08.001.
[6] H. Zhang, H. Zhu, T. Qi, Z. Hu, X. Zeng, Selective laser melting of high strength Al – Cu – Mg alloys : processing, microstructure and mechanical properties, Mater. Sci. Eng. A 656 (2016) 47–54, https://doi.org/10.1016/j.msea.2015.12.101.
[7] M.B.K. Kempen, L. Thijs, E. Yasa, Process Optimization and Microstructural Analysis for Selective Laser, (2011), pp. 484–495.
[8] D. Buchbinder, W. Meiners, K. Wissenbach, R. Poprawe, Selective laser melting of aluminum die-cast alloy—correlations between process parameters, solidification conditions, and resulting mechanical properties, J. Laser Appl. 27 (2015), https://doi.org/10.2351/1.4906389 S29205.
[9] T. Kimura, T. Nakamoto, Microstructures and mechanical properties of A356 (AlSi7Mg0.3) aluminum alloy fabricated by selective laser melting, JMADE 89 (2016) 1294–1301, https://doi.org/10.1016/j.matdes.2015.10.065.
[10] D. Buchbinder, H. Schleifenbaum, S. Heidrich, M. W, J. Bultmann, High power selective laser melting (HP SLM) of aluminum parts, Phys. Procedia 12 (2011) 271–278, https://doi.org/10.1016/j.phpro.2011.03.035.
[11] H. Rao, S. Giet, K. Yang, X. Wu, C.H.J. Davies, The influence of processing parameters on aluminium alloy A357 manufactured by selective laser melting, Mater. Des. 109 (2016) 334–346, https://doi.org/10.1016/j.matdes.2016.07.009.
[12] N. Read, W. Wang, K. Essa, M.M. Attallah, Selective laser melting of AlSi10Mg alloy: Process optimisation and mechanical properties development, Mater. Des. 65 (2015) 417–424, https://doi.org/10.1016/j.matdes.2014.09.044.
[13] E.C. Santos, M. Shiomi, K. Osakada, T. Laoui, Rapid manufacturing of metal components by laser forming, Int. J. Mach. Tools Manuf. 46 (2006) 1459–1468, https://doi.org/10.1016/j.ijmachtools.2005.09.005.
[14] E.O. Olakanmi, R.F. Cochrane, K.W. Dalgarno, A review on selective laser sintering / melting (SLS / SLM) of aluminium alloy powders: processing, microstructure, and properties, J. Prog. Mater. Sci. 74 (2015) 401–477, https://doi.org/10.1016/j.pmatsci.2015.03.002.
[15] W.C. Dalgarno, K. W, Approaches to processing metals and ceramics through the laser scanning of powder beds – a review, Powder Met. Prog. 1 (1) (2001) 70–79.
[16] R.H. Morgan, A.J. Papworth, C. Sutcliffe, P. Fox, W. O'Neill, High density net shape components by direct laser re-melting of single-phase powders, J. Mater. Sci. 37 (2002) 3093–3100, https://doi.org/10.1023/A:1016185606642.
[17] H.K. O'Neill W, C.J. Sutcliffe, R. Morgan, A. Landsborough, Investigation on multi-layer direct metal laser sintering of 316L stainless steel powder beds, Ann CIRP 48 (1) (1999) 151–154, https://doi.org/10.1016/S0007-8506(07)63153-9.
[18] J.P. Kruth, L. Froyen, J. Van Vaerenbergh, P. Mercelis, M. Rombouts, B. Lauwers, Selective laser melting of iron-based powder, J. Mater. Process. Technol. 149 (2004) 616–622, https://doi.org/10.1016/j.jmatprotec.2003.11.051.
[19] P. Fischer, M. Locher, V. Romano, H.P. Weber, S. Kolossov, R. Glardon, Temperature measurements during selective laser sintering of titanium powder, Int. J. Mach. Tools Manuf. 44 (2004) 1293–1296, https://doi.org/10.1016/j.ijmachtools.2004.04.019.
[20] X. Zhou, X. Liu, D. Zhang, Z. Shen, W. Liu, Balling phenomena in selective laser melted tungsten, J. Mater. Process. Technol. 222 (2015) 33–42, https://doi.org/10.1016/j.jmatprotec.2015.02.032.
[21] L. Wang, S. Wang, J. Wu, Experimental investigation on densification behavior and surface roughness of AlSi10Mg powders produced by selective laser melting, Opt. Laser Technol. 96 (2017) 88–96, https://doi.org/10.1016/j.optlastec.2017.05.006.
[22] X. Ding, L. Wang, Heat transfer and fluid flow of molten pool during selective laser melting of AlSi10Mg powder: simulation and experiment, J. Manuf. Process. 26 (2017) 280–289, https://doi.org/10.1016/j.jmapro.2017.02.009.
[23] X. Ding, L. Wang, S. Wang, Comparison study of numerical analysis for heat transfer and fluid flow under two different laser scan pattern during selective laser melting, Opt. – Int. J. Light Electron. Opt. 127 (2016) 10898–10907, https://doi.org/10.1016/j.ijleo.2016.08.123.
[24] L. Caprio, A.G. Demir, B. Previtali, Comparative study between CW and PW emissions in selective laser melting, J. Laser Appl. (2018) 30–33 032305/1-8.
[25] R. Casati, J. Fiocchi, A. Fabrizi, N. Lecis, F. Bonollo, M. Vedani, Effect of ball milling on the ageing response of Al2618 composites reinforced with SiC and oxide nanoparticles, J. Alloys. Compd. 693 (2017), https://doi.org/10.1016/j.jallcom.2016.09.265.
[26] J.M. Criado, A. Ortega, Non-isothermal transformation kinetics: remarks on the Kissinger method, J. Non. Solids 87 (1986) 302–311, https://doi.org/10.1016/S0022-3093(86)80004-7.

[27] M. Starink, The determination of activation energy from linear heating rate experiments: a comparison of the accuracy of isoconversion methods, Thermochim. Acta 404 (2003) 163–176, https://doi.org/10.1016/S0040-6031(03)00144-8.
[28] M.J. Starink, On the applicability of isoconversion methods for obtaining the activation energy of reactions within a temperature-dependent equilibrium state, J. Mater. Sci. 32 (1997) 6505–6512, https://doi.org/10.1023/A:1018655026036.
[29] L.V. Meisel, P.J. Cote, Non-isothermal transformation kinetics: application to metastable phases, Acta Metall. 31 (1983) 1053–1059, https://doi.org/10.1016/0001-6160(83)90201-8.
[30] J. Fiocchi, A. Tuissi, P. Bassani, C.A. Biffi, Low temperature annealing dedicated to AlSi10Mg selective laser melting products, J. Alloys. Compd. 695 (2017) 3402–3409, https://doi.org/10.1016/j.jallcom.2016.12.019.
[31] T.B. Massalski, William W. ScottJr (Ed.), Binary Alloys Phase Diagrams, 2nd ed., 1990.
[32] ASTM standards, E112: Standard Test Methods for Determining Average Grain Size, (1996), https://doi.org/10.1520/E0112-12.
[33] C.A. Biffi, J. Fiocchi, A. Tuissi, Selective laser melting of AlSi10 Mg: Influence of process parameters on Mg2Si precipitation and Si spheroidization, J. Alloys. Compd. 755 (2018) 100–107, https://doi.org/10.1016/j.jallcom.2018.04.298.
[34] M. van Rooyen, E.J. Mittemeijer, Precipitation of silicon in aluminum-silicon: a calorimetric analysis of liquid-quenched and solid-quenched alloys, Metall. Trans. A 20 (1989) 1207–1214, https://doi.org/10.1007/BF02647402.
[35] P. Van Mourik, E.J. Mittemeijer, T.H. De Keijser, On precipitation in rapidly solidified aluminium-silicon alloys, J. Mater. Sci. 18 (1983) 2706–2720, https://doi.org/10.1007/BF00547587.
[36] G. Thomas, R.H. Willens, Defects in aluminum quenched from the liquid state*, Acta Metall. 12 (1964) 191–196.